

## Zero-field Optic Mode Beyond 20 GHz in a Synthetic Antiferromagnet

H. J. Waring<sup>1,\*</sup>, N. A. B. Johansson,<sup>1</sup> I. J. Vera-Marun<sup>1,2</sup>, and T. Thomson<sup>1</sup>

<sup>1</sup>*Nano-Engineering and Spintronic Technologies (NEST), Department of Computer Science, University of Manchester, Manchester, UK*

<sup>2</sup>*Department of Physics and Astronomy, University of Manchester, Manchester, UK*

(Received 2 December 2019; revised manuscript received 31 January 2020; accepted 3 February 2020; published 13 March 2020)

Antiferromagnets have considerable potential as spintronic materials. Their dynamic properties include resonant modes at frequencies higher than can be observed in conventional ferromagnetic materials. An alternative to single-phase antiferromagnets are synthetic antiferromagnets (SAFs), engineered structures of exchange-coupled ferromagnet/nonmagnet/ferromagnet trilayers. SAFs have significant advantages due to the wide-ranging tunability of their magnetic properties and inherent compatibility with current device technologies, such as those used for Spin-transfer-torque magnetic random-access memory production. Here we report the dynamic properties of fully compensated SAFs using broadband ferromagnetic resonance and demonstrate resonant optic modes in addition to the conventional acoustic (Kittel) mode. These optic modes possess the highest zero-field frequencies observed in SAFs to date with resonances of 18 and 21 GHz at the first and second peaks in antiferromagnetic Ruderman-Kittel-Kasuya-Yosida (RKKY) coupling, respectively. In contrast to previous SAF reports that focus only on the first RKKY antiferromagnetic coupling peak, we show that a higher optic mode frequency is obtained for the second antiferromagnetic coupling peak. We ascribe this to the smoother interfaces associated with a thicker non-magnetic layer. This demonstrates the importance of interface quality to achieving high-frequency optic mode dynamics entering the subterahertz range.

DOI: 10.1103/PhysRevApplied.13.034035

### I. INTRODUCTION

Antiferromagnetic (AF) spintronics has recently become a key area of research to enhance the capabilities of spintronic devices [1,2]. They are increasingly poised to augment or even replace current ferromagnetic components across a range of technologies, a remarkable resurgence given the description of “interesting and useless” bequeathed to this class of materials by Néel [3]. Due to their characteristic antiparallel spin ordering, antiferromagnets (AFMs) have a low or zero net magnetization, eliminating the stray field responsible for promoting thermal activation of reversal and hence offering advantages in data storage such as magnetic random-access memories (MRAM) [4], Spin-transfer-torque magnetic random-access memory (STT MRAM) [5], and magnetic sensors [6]. Furthermore, their dynamic response can reach towards the terahertz range, orders of magnitudes higher than the low-gigahertz range typically found

in ferromagnets, leading to the possibility of engineering higher-frequency devices than used currently [1,7,8]. Most antiferromagnets found in nature are also dielectrics, which contributes to the elimination of Joule heating [9–11]. However, metallic AFMs and particularly those where there is freedom to design the required properties can offer advantages, for example, when there is a need for layer thicknesses below 10 nm.

Magnetic materials are essential components of high-frequency technologies and devices. The maximum speed of operation and frequency range of magnetic materials is determined by the ferromagnetic resonance frequency,  $f_r$  [12,13]. To realize gigahertz-range magnetic devices it is essential to engineer materials that support a much greater  $f_r$  [14]. The resonant frequency of ferromagnetically ordered materials is given by Kittel’s equation [15],

$$f_r^A = \frac{\gamma}{2\pi} \sqrt{(H + H_k)(H + H_k + 4\pi M_s)}, \quad (1)$$

where  $f_r^A$  is the conventional acoustic mode ferromagnetic resonance,  $\gamma$  is the gyromagnetic ratio,  $H$  is the applied magnetic field,  $H_k$  is the uniaxial anisotropy, and  $M_s$  is the saturation magnetization. Resonant frequencies can be increased through the application of large magnetic

\*harry.waring@manchester.ac.uk

Published by the American Physical Society under the terms of the [Creative Commons Attribution 4.0 International license](#). Further distribution of this work must maintain attribution to the author(s) and the published article’s title, journal citation, and DOI.

fields, with notable examples including resonant frequencies nearing 100 GHz with applied fields of around 5 T in Co-Cr-Pt-Ta thin films, as demonstrated by Oates *et al.* [16]. However, for future device development, it is critical to consider miniaturization and heat management [9], which makes the application of large magnetic fields technically challenging. It is therefore desirable for magnetic materials to possess a very high self-bias, meaning no externally applied magnetic field is required to achieve higher resonance frequencies. Conventional methods of accomplishing this goal involve using materials with a high-saturation magnetization  $4\pi M_s$  or increasing  $H_k$ . From a material selection point of view, the focus of the community has pivoted toward ferrites such as CoFe-based materials [17–19]. Enhancements to  $H_k$  are typically achieved through the application of a magnetic field during deposition with potential use of annealing [20], tailoring the nanocrystalline structure of the films using chemical stress or oblique sputtering [17,21], use of prestressed substrates [22], or lamination and lithographic patterning [14]. Exchange-biased systems have also been proposed [23]. The highest frequencies in self-bias systems achieved to date are in the  $X$ -band range, around 10 GHz [17,23]. There are notable difficulties in further tailoring of  $H_k$  using the methods outlined above, such as the application of a dc field during depositions, which induces an anisotropy that is difficult to modify and prestressed substrates requiring mechanical flexibility.

The limitations in achieving further increases of  $H_k$  to realize higher-frequency magnetic devices have led to the exploitation of AF materials that have faster dynamic responses than are available in their ferromagnetic counterparts [1,7,24]. Resonance experiments of single-phase antiferromagnets are typically conducted with terahertz-range optical or electrical field probing techniques [8,25–29], with limited reports of antiferromagnets with dynamics in the range of conventional microwave electronics [30]. Therefore, there is a particular research interest in synthetic antiferromagnetic (SAF) structures, comprised of an exchange-coupled ferromagnet-nonmagnet-ferromagnet (FM-NM-FM) multilayers. However, as the interlayer exchange coupling ( $J_{IEC}$ ) seen in SAFs is smaller than the direct exchange coupling seen in single-phase antiferromagnets, the resonance frequencies are also reduced. This opens up additional possibilities for AFM-based devices, extending the range of frequencies that can be generated, and provides a method to tailor the frequency obtained through controlling the coupling interaction [31,32]. The interlayer coupling results from the Ruderman-Kittel-Kasuya-Yosida (RKKY) interaction [33], which for an appropriate choice of spacer layer such as Ru is responsible for an oscillatory short-range interaction that can promote ferromagnetic or antiferromagnetic layer alignment depending on spacer layer thickness. Here the nonmagnetic spacer layer is chosen to produce a

configuration where the magnetizations of the FM layers align antiparallel. In effect, the RKKY interaction creates spin density oscillations in the NM spacer layer as its thickness is altered. The strength and period of the RKKY coupling is highly sensitive to the Fermi surface of the NM metal [33,34]. In particular, it is found that the periodicity of the coupling is given by

$$\Lambda = \frac{1}{|(1/\lambda) - (n/d)|}, \quad (2)$$

where  $\lambda$  is the Fermi wavelength,  $d$  is half the lattice parameter of the spacer material, and  $n$  is a positive integer satisfying the criterion  $\Lambda \geq 2d$  [35].

The presence of this interlayer coupling has a significant impact on the precessional dynamics of the SAF system. Here the resonance frequency is enhanced by the addition of an effective interlayer coupling term ( $H_{ex}$ ) in the dispersion relation that introduces an optic mode resonance ( $f_r^o$ ) in the AF configuration [36], shown schematically in Fig. 1 and given by

$$f_r^o = \frac{\gamma}{2\pi} \sqrt{(H + H_{ex} + H_k)(H + H_{ex} + H_k + 4\pi M_s)}. \quad (3)$$

This optic mode has been studied by several groups due to its potential to significantly enhance self-biased ferromagnetic resonances towards low-terahertz frequencies [36]. In recent works, notable enhancements to the  $f_r$  frequency were demonstrated by Li *et al.* [37] who reported a zero-field optic mode resonance of 11.32 GHz. Further, SAFs fabricated using a range of ferromagnetic components have been explored including Ni-Fe [38], Co [39,40] and (Fe,Co)N [41]. Additionally, ferromagnetic components created from highly spin-polarized Heusler alloys such as Co<sub>2</sub>FeAl have been reported [42].

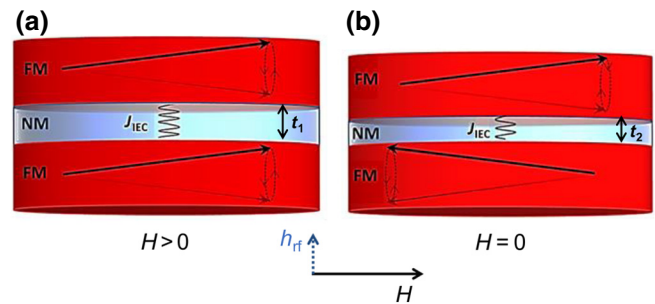
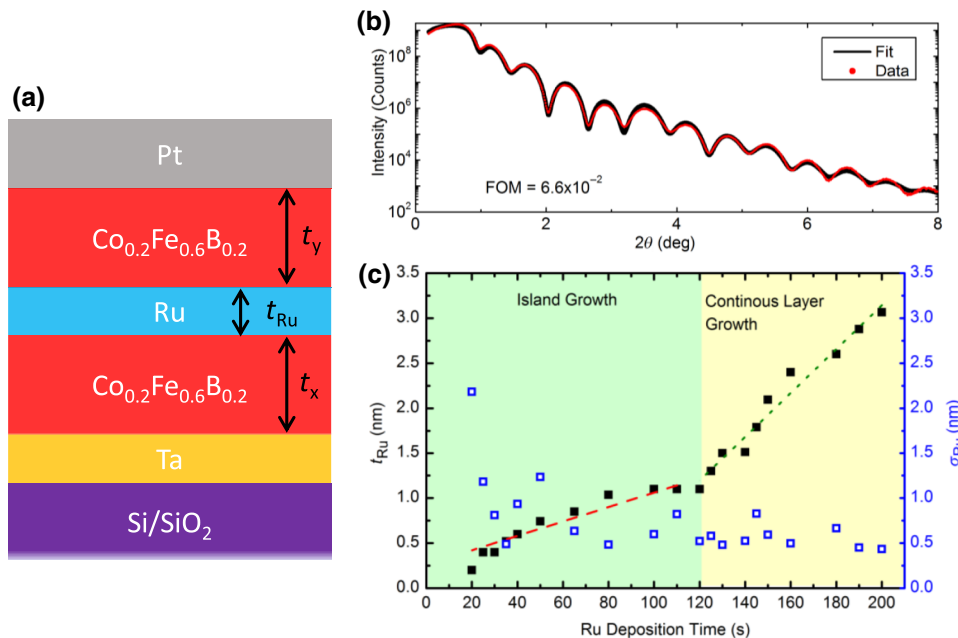


FIG. 1. Magnetic precession of an FM-NM-FM trilayer system due to a perturbation field  $h_{rf}$  when (a) NM thickness  $t_1$  promotes a ferromagnetic alignment, and (b) NM thickness  $t_2$  promotes an antiferromagnetic alignment. A field  $H$  needs to be applied to (a) to enable similar high resonant frequencies to that displayed at zero field in (b). The red-colored layers are ferromagnetic, while the blue is the nonmagnetic spacer layer.

In this work, we demonstrate that higher frequencies (in excess of 20 GHz) can be obtained for the zero-field optic mode using SAFs with the structure  $\text{Co}_{0.2}\text{Fe}_{0.6}\text{B}_{0.2}(5 \text{ nm})/\text{Ru}(t_{\text{Ru}})/\text{Co}_{0.2}\text{Fe}_{0.6}\text{B}_{0.2}(5 \text{ nm})$ , where  $t_{\text{Ru}}$  is the Ru layer thickness. The  $\text{Co}_{0.2}\text{Fe}_{0.6}\text{B}_{0.2}$  layer thicknesses are chosen to be comparable to the exchange length, which ensured that each layer is, internally, strongly exchange coupled. The samples exhibit large effective interlayer coupling strengths  $H_{\text{ex}}$  that are among the highest seen to date, which leads directly to a high self-bias  $f_r$ . We show that the second RKKY AF coupling peak supports faster precessional dynamics than the first peak and explore the correlation between Ru layer interface quality and interlayer coupling strength.

## II. SAMPLE PREPARATION AND CHARACTERIZATION

A series of samples are produced using magnetron sputtering on to  $\text{Si}/\text{SiO}_2$  substrates (see Appendix A1). The multilayer structure is  $\text{Ta}(2 \text{ nm})/\text{Co}_{0.2}\text{Fe}_{0.6}\text{B}_{0.2}(5 \text{ nm})/\text{Ru}(t_{\text{Ru}})/\text{Co}_{0.2}\text{Fe}_{0.6}\text{B}_{0.2}(5 \text{ nm})/\text{Pt}(4 \text{ nm})$ . Ru is chosen as the spacer layer material due to the strong interlayer coupling it can support [34].  $\text{Co}_{0.2}\text{Fe}_{0.6}\text{B}_{0.2}$  is selected as the ferromagnetic component as significant literature exists on the high-frequency properties of Co-Fe alloys containing B [17,18,43–45]. Ta is used as a seed layer, with Pt or Pd used as a capping layer to inhibit oxidization of the films. An extensive optimization process is undertaken where dc sputtering power is reduced to ensure smooth layer growth throughout the structure, with rf sputtering used for the Ru layer to achieve precise control over nonmagnetic layer growth (see Appendix A1).

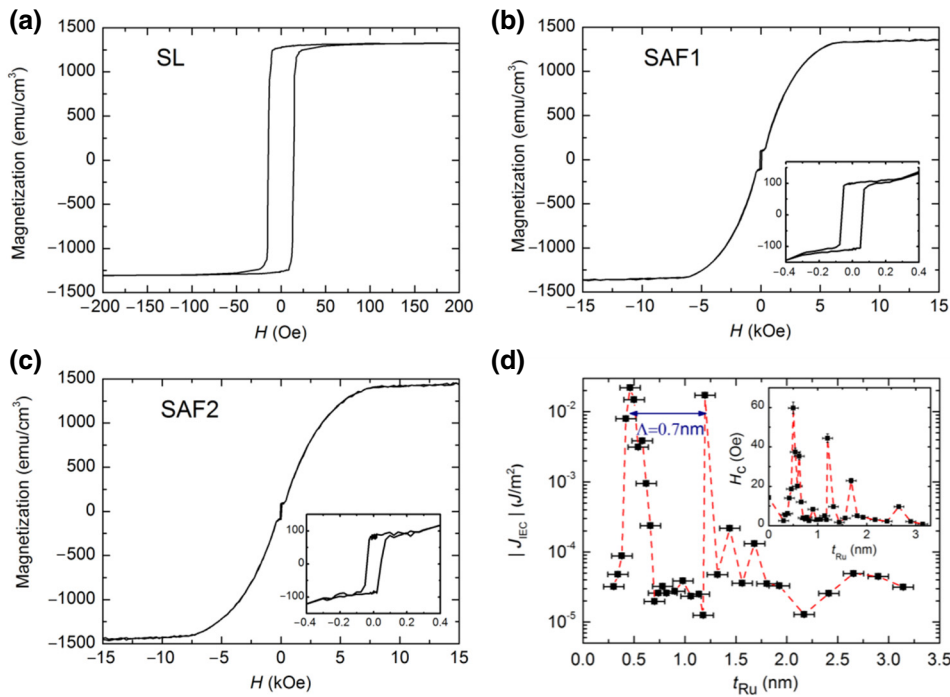


The layer structure of the multilayers, shown in Fig. 2(a), is determined using X-ray reflectivity (XRR) where the data are fitted to a Fresnel model using the GENX software package (see Appendix B1), with an example fit presented in Fig. 2(b). The data for a series of films where the Ru thickness is varied while the layer thicknesses of the  $\text{Co}_{0.2}\text{Fe}_{0.6}\text{B}_{0.2}$  FM layers are kept constant are summarized in Fig. 2(c). It can be seen that two distinct growth regimes are observed as Ru layer thickness increases. These data support a hypothesis of an initial island growth stage that subsequently coalesces to form a continuous Ru film at approximately 1-nm thickness. The roughness of the Ru layer decreases with deposition time [Fig. 2(c)], as expected from this growth model. The average roughness in the island growth regime is 1.1 nm and in the continuous regime it is 0.6 nm. Antiferromagnetic coupling is found in the case of  $t_{\text{Ru}} = 0.6 \text{ nm}$  and  $t_{\text{Ru}} = 1.1 \text{ nm}$ , which are referred to as SAF1 and SAF2 respectively. The properties of a single  $\text{Co}_{0.2}\text{Fe}_{0.6}\text{B}_{0.2}$  layer, structure  $\text{Ta}(2 \text{ nm})/\text{Co}_{0.2}\text{Fe}_{0.6}\text{B}_{0.2}(9 \text{ nm})/\text{Pt}(4 \text{ nm})$ , is also presented and referred to as SL.

## III. STATIC MAGNETIC PROPERTIES

Vibrating sample magnetometry (VSM) is used to determine the static magnetic properties (see Appendix B2).  $M$ - $H$  hysteresis loops for the SL, SAF1, and SAF2 samples are presented in Fig. 3, which demonstrates the changing magnetic characteristics of the films with increases in Ru thickness. In the case of SAF1 and SAF2, an AF coupling between the FM layers means that as the external field is decreased, the magnetization decreases until a plateau is reached, where an antiparallel alignment of the layers is achieved. The finite value of magnetization for this plateau

FIG. 2. Stack structure characterization. (a) A schematic diagram of the overall stack structure. (b) An example XRR data set and fit for a stack with Ru thickness ( $t_{\text{Ru}} = 1.1 \text{ nm}$ ) where the figure of merit (FOM) obtained for the fit is shown. (c) Thickness and associated roughness ( $\sigma_{\text{Ru}}$ ) of the Ru layer for a range of deposition times. The dashed lines are a guide to the eye.



is due to minor differences between the two FM layers that are experimentally unavoidable. The saturating field for SAF1 is around 5 kOe, while for SAF2 it is around 6.5 kOe. This is significantly greater than the approximate value of 2 kOe reported in previous works [21], leading to the conclusion that these samples also display large interlayer coupling strengths ( $J_{\text{IEC}}$ ), and demonstrate a high  $H_{\text{ex}}$  [41]. Figure 3(d) shows the interlayer coupling as a function of Ru thickness, with the first and second AF RKKY interaction peaks observed at  $t_{\text{Ru}} = 0.6 \text{ nm}$  and  $t_{\text{Ru}} = 1.1 \text{ nm}$ . The effective interlayer coupling strength  $H_{\text{ex}}$  is calculated using [21]

$$H_{\text{ex}} = \frac{2 J_{\text{IEC}}}{M_S (t_x + t_y)}, \quad (4)$$

where  $t_x$  and  $t_y$  are the thicknesses of the two FM layers and  $J_{\text{IEC}}$  is given by

$$J_{\text{IEC}} = M_S H_{\text{Sat}} \frac{t_x t_y}{t_x + t_y}, \quad (5)$$

where  $H_{\text{Sat}}$  is the saturating external field [46].

The coercive field versus Ru thickness is plotted in Fig. 3(d) (inset), which demonstrates that the AF coupling is correlated with an increase in the coercive field ( $H_c$ ). This behavior is easily understood as AF coupling provides an additional energy term ( $J_{\text{IEC}}$ ) that must be overcome to align the system ferromagnetically with an applied magnetic field. The measured oscillation period compares well with expectations in the literature [47], and the theoretical period is calculated to be 0.5 nm from Eq. (2), while the

FIG. 3.  $M$ - $H$  hysteresis loops of: (a) single  $\text{Co}_{0.2}\text{Fe}_{0.6}\text{B}_{0.2}$  layer (SL); (b) synthetic antiferromagnet with interlayer coupling on first antiferromagnetic peak (SAF1); (c) synthetic antiferromagnet with interlayer coupling on second antiferromagnetic peak (SAF2). The inserts in (b) and (c) show the low-field behavior plotted on the same scale. (d) Magnitude of the interlayer exchange coupling ( $J_{\text{IEC}}$ ) of the trilayers with varying thicknesses of Ru ( $t_{\text{Ru}}$ ) acting as spacer layer. The measured wavelength ( $\Lambda$ ) of RKKY interaction is also presented. Inset: coercive field ( $H_c$ ) of the trilayers with varying  $t_{\text{Ru}}$ .

experimentally determined value is  $\Lambda \sim 0.7 \text{ nm}$ . The difference between these values is mostly likely caused by the effects of interfacial roughness as it has been shown that roughness can have the effect of broadening the interlayer coupling peaks and introducing an asymmetry [33]. The RKKY interaction is expected to be strongest at the first AF coupling peak [34]. However, these data show that  $J_{\text{IEC}}$  is only slightly reduced at the second AF coupling peak. We ascribe this to the smoother Ru interface, as shown in Fig. 2(c). This suggests that improvements in film growth could further increase AF coupling strength.

#### IV. DYNAMIC MAGNETIC PROPERTIES

Dynamic properties are measured using a broadband vector network analyzer ferromagnetic resonance spectrometer (VNA FMR) at room temperature with the magnetic field applied along the plane of the samples (see Appendix B3). The resonance is characterized using the VNA  $S_{12}$  absorption parameter. Figures 4(a)–4(c) show examples of individual spectra measured using applied magnetic fields of 0 Oe, 1 kOe, and 8 kOe for each of the samples investigated. These applied magnetic field values are chosen to demonstrate the dynamic properties of the range of magnetic configurations attainable in these SAF structures. In the case of SL [Fig. 4(a)] only a conventional acoustic mode (AM) is measured as expected, while in the case of SAF1 [Fig. 4(b)] and SAF2 [Fig. 4(c)] both acoustic and optic modes (OM) are present. Figures 4(d)–4(f) show two-dimensional maps of the resonance spectra as a function of applied field and frequency. These data exhibit a range of frequencies over which both the AM (Kittel

mode) and the OM occur, and demonstrate a zero-field OM of  $18.2 \pm 1.2$  GHz in the case of the first AF maximum (sample SAF1) and  $21.13 \pm 0.01$  GHz at the second AF maximum (sample SAF2), contrasting with the zero-field SL resonance of  $2.8 \pm 0.1$  GHz, which is due to the presence of a finite  $H_k$ . In order to analyze these spectra in more detail we consider three regions that are determined by the applied magnetic field. In the high field (region I) of SAF1 and SAF2 and at all field values in the SL sample we find only the expected AM resonance. As the applied field is reduced (in magnitude) a dual mode exists (region II) where the magnetization vectors are reorienting from a parallel to antiparallel alignment, while for low applied fields (region III) only the OM associated with antiparallel alignment is obtained. An acoustic mode is not seen in the AF configuration due to these vectors resonating in phase but in opposite direction canceling out any measurable response (essentially phase locked) [21,48]. The experimental data show that the optic mode endures to much higher fields than has been reported previously, vanishing at an applied field of approximately 1400 Oe in the case of SAF2 as opposed to the approximately 300 Oe field value seen in other literature reports [49].

The VNA FMR experiment also allows the linewidth of the resonances shown in Figs. 4(a)–4(c) to be determined. Figure 5 shows how these linewidths vary with applied field for the OM of both SAF1 and SAF2. It is likely that the difference in resonant linewidth exhibited by SAF1 and SAF2 is correlated to the observed change in Ru growth mode and layer roughness from SAF1 to SAF2, as demonstrated by Fig. 2(c). However, to verify this hypothesis more detailed simulations than the simple analytical models we report here are required.

## V. MODELING

In order to study the resonant modes of the SAF samples we employ a simple analytical model for coupled magnetic thin-film trilayers developed by Rezende *et al.* [50] and Wigen *et al.* [50,51]. The model describes the resonant modes of a SAF structure undergoing a spin-flop process from an antiferromagnetic to ferromagnetic alignment, consistent with the dynamic behavior displayed in these data. Mathematically, for increasing field the onset of the spin-flop regime (region II), where the magnetic vectors commence reorientation from antiparallel (region III) to parallel alignment (region I), starts at  $H_{SF}$ , defined as

$$H_{SF} = \sqrt{H_k(2H_{ex} + H_k)}, \quad (6)$$

with the field necessary to align the magnetization of each layer defined as

$$H_{sat} = 2H_{ex} - H_k. \quad (7)$$

The angle of the magnetization vectors during the reorientation from antiferromagnetic to ferromagnetic alignment with increasing field is defined as

$$\sin \theta = \frac{H}{2H_{ex} - H_k}, \quad (8)$$

where  $\theta$  is the angle of the magnetization vectors from the easy axis of the in-plane anisotropy, which is also the direction along which  $H$  is applied. In the case of the antiferromagnetically coupled regime ( $H < H_{SF}$ ), the expected resonant frequencies are given by

$$f_{\pm} = \frac{\gamma}{2\pi} \sqrt{H^2 - H_k^2 + (H_k + H_{ex})(2H_k + 4\pi M_s) \pm \left[ \frac{H^2(2H_k + 4\pi M_s)(2H_k + 4\pi M_s + 4H_{ex}) + H_{ex}^2(4\pi M_s)^2}{H_{ex}^2(4\pi M_s)^2} \right]^{1/2}}, \quad (9)$$

where  $f_+(f_-)$  is the optic (acoustic) mode resonant frequency. In the spin-flop region ( $H_{SF} < H < H_{sat}$ ), the resonant frequencies are given by

$$f_{\pm} = \frac{\gamma}{2\pi} \sqrt{[2H_{ex}^2 + H_k(H_{ex} + 4\pi M_s)]\sin^2 \theta + (H_{ex} + 4\pi M_s)(H_{ex} - H_k) - H_{ex}^2 \pm H_{ex} \left[ \frac{(2H_{ex} + 8\pi M_s + H_k)\sin^2 \theta}{-(H_k + 4\pi M_s)} \right]}, \quad (10)$$

where, conversely,  $f_+(f_-)$  is the modeled acoustic (optic) mode resonant frequency. In the saturated regime ( $H > H_{sat}$ ), the acoustic mode is described by Eq. (1) with an OM resonance given by a slight modification to this equation incorporating  $H_{ex}$ :

$$f_r^o = \frac{\gamma}{2\pi} \sqrt{(H + H_k - 2H_{ex})(H + H_k - 2H_{ex} + 4\pi M_s)}. \quad (11)$$

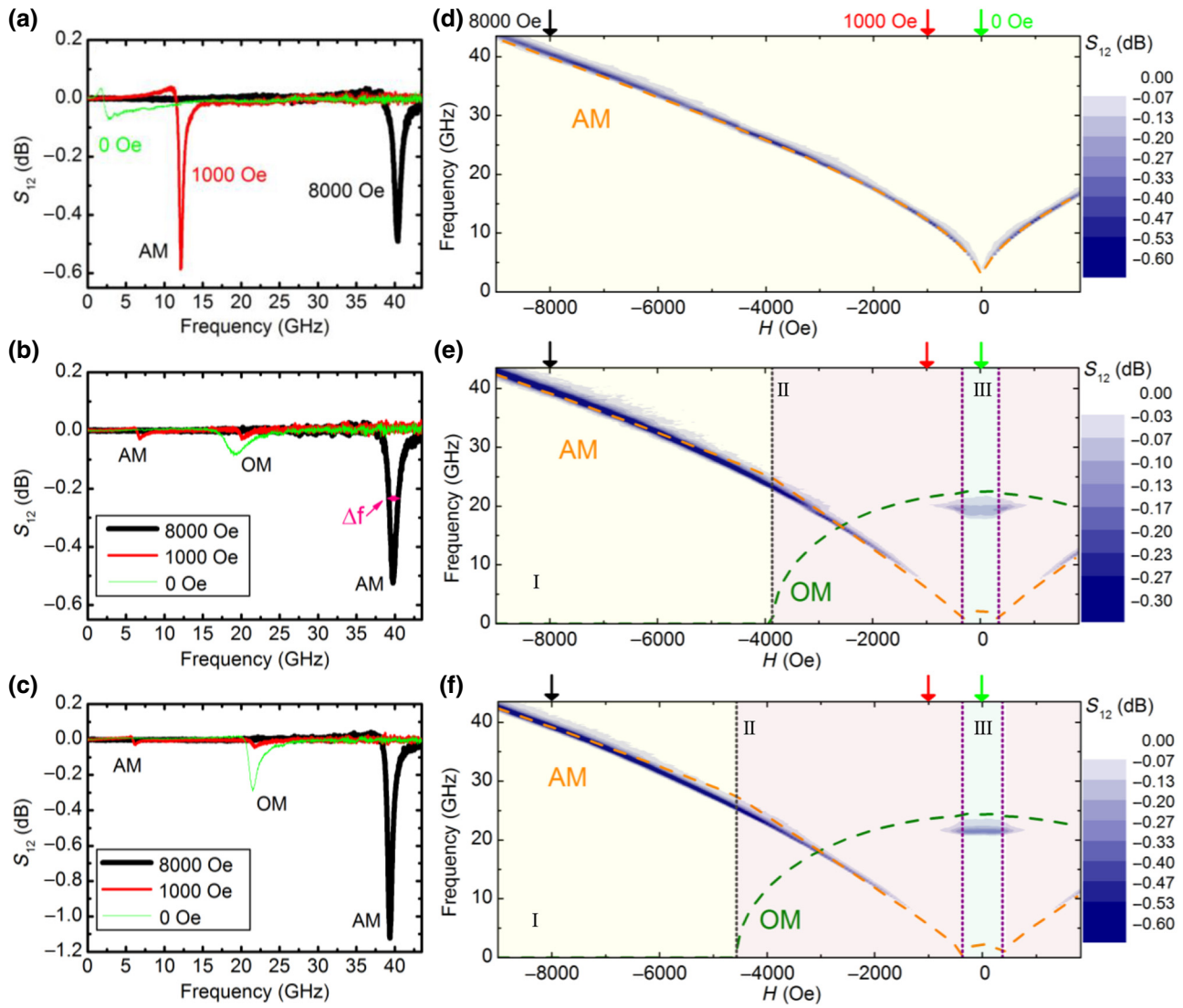


FIG. 4.  $S_{12}$  absorption profiles for different applied fields for (a) single-layer  $\text{Co}_{0.2}\text{Fe}_{0.6}\text{B}_{0.2}$  (SL), (b) synthetic antiferromagnet with interlayer coupling on the first antiferromagnetic RKKY peak (SAF1), and (c) synthetic antiferromagnet with interlayer coupling on the second antiferromagnetic RKKY peak (SAF2). The resonant linewidth ( $\Delta f$ ) is highlighted. Two-dimensional maps of the resonant spectra and modeled behavior (dashed lines) of the acoustic mode (AM) and optic mode (OM) are displayed for (d) SL, (e) SAF1, and (f) SAF2. The three magnetization regimes are highlighted: region I where the magnetizations of the layers are ferromagnetically aligned, region II where the magnetization of each layer are undergoing a spin-flop reorientation, and region III where the magnetizations are in an antiferromagnetic configuration.

As shown in Figs. 4(d)–4(f), this simple model successfully reproduces the major features of the measured resonances, with parameter optimization performed using a least-squares fitting procedure between the modeled and measured Kittel mode present in the saturated and spin-flop regime. The functional forms of the acoustic and optic modes are very well described by the model. However, the modeled OM frequency is higher by 22% and 16% for SAF1 and SAF2, respectively. The simple model also does not capture the behavior of the OM throughout the spin-flop phase (region II) with a field insensitive

resonance with diminishing intensity observed experimentally. It is hypothesized that these differences are due to additional contributions to the resonant dynamics of the spin-flop and antiparallel regimes beyond that accounted for in the parameters of the model, such as spin pumping or the role of lateral spin transport due to local variations in the interfaces present within the system [52,53].

The parameters obtained from the model are presented in Table I. This approach allows values for  $H_k$  and  $H_{\text{ex}}$  to be obtained that are typically difficult to deconvolute.

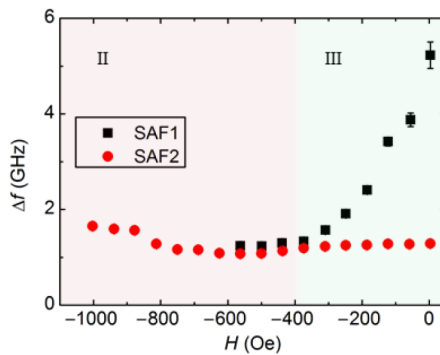


FIG. 5. Resonant linewidths ( $\Delta f$ ) of the optic modes of synthetic antiferromagnets with interlayer coupling on the first antiferromagnetic RKKY peak (SAF1) and on the second antiferromagnetic RKKY peak (SAF2). The two magnetization regimes where an optic is present are highlighted: region III where the magnetizations of the layers are antiferromagnetically aligned, and region II where the magnetization of each layer is undergoing a spin-flop reorientation. Error bars are within the symbols for some data.

The fitted FMR data shows that two characteristics are needed to achieve enhanced optic mode resonant frequencies: namely an in-plane uniaxial anisotropy and RKKY coupling between the two FM layers. The effective interlayer couplings  $H_{\text{ex}}$  extracted from the model of the FMR data are only slightly lower than those expected from VSM measurements. This supports the analytical extraction of  $H_{\text{ex}}$  from the static and dynamic measurements. The closer agreement between these two values for SAF1 than for SAF2 could possibly be due to dynamic effects that may influence higher-frequency dynamic behavior to a greater degree, such as phenomena related to spin transport.

The model also predicts the presence of a small in-plane uniaxial anisotropy, which has also been experimentally observed from rotational VSM measurements (see Supplemental Material [54]). The model of the acoustic mode for SAF1 and SAF2 indicates that  $H_k$  is approximately half the value of that found for the SL. Hence, uniaxial anisotropy is present in all samples, although no deliberate conditions are employed to induce anisotropy. It can therefore be concluded that this is likely to be an intrinsic property of the material [55]. Analysis of the Landé  $g$

TABLE I. Parameters obtained from fitting the FMR data to the analytical model proposed by Rezende *et al.* [50]. The effective coupling from VSM measurement is found using Eqs. (4) and (5).

Sample	$g$	$M_s$ (emu/cm <sup>3</sup> )	$H_k$ (Oe)	FMR: $H_{\text{ex}}$ (Oe)	VSM: $H_{\text{ex}}$ (Oe)
SL	2.03	1300	58	—	—
SAF1	2	1300	30	1950	1980
SAF2	2	1300	30	2300	2580

factor shows that a value of 2.03 provides a better fit to the single-film dynamics whereas a value of 2.00, the lower boundary, is optimum in the case of the SAF systems. This reduction is possibly due to breaking of inversion symmetry through the inclusion of an Ru layer or intermixing of ferromagnetic layer with nonmagnetic Ru [56].

## VI. CONCLUSION

In summary, we demonstrate the highest optic mode resonant frequencies in synthetic antiferromagnets at zero applied magnetic field reported to date. The measured resonant frequencies at zero field are  $18.2 \pm 1.2$  GHz and  $21.13 \pm 0.01$  GHz for samples on the first and second antiferromagnetic peaks of the RKKY interaction, respectively. This represents approximately an order-of-magnitude increase compared to the resonance frequency of a single  $\text{Co}_{0.2}\text{Fe}_{0.6}\text{B}_{0.2}$  layer,  $2.8 \pm 0.1$  GHz. The individual ferromagnetic layers are significantly thinner than those previously reported [37], which could result in a smaller signal output when incorporated into a device architecture. A simple analytical model is remarkably successful at reproducing all the major features of the SAF resonances. The parameters obtained from the model also show good agreement with the data, but some differences are found for  $H_{\text{ex}}$  and  $H_{\text{sat}}$  when compared with the values expected from static (VSM) measurements. The SAFs possess both in-plane uniaxial anisotropy and interlayer coupling, which are essential components to achieve high-frequency optic mode resonances. This work has shown that smoother  $(\text{Co},\text{Fe})\text{B}$ -Ru interfaces offers one route to key technological improvement. The correlation of structural, static, and dynamic characterizations highlights the use of the second, and potentially also higher-order, antiferromagnetic peaks to drive the self-bias resonance frequency of synthetic antiferromagnetic systems into the subterahertz range.

## ACKNOWLEDGMENTS

The authors gratefully acknowledge the support of the UK EPSRC CDT Graphene NOWNANO through Grant No. EP/L01548X/1 and the involvement of the facilities of the Henry Royce Institute through EPSRC Grants No. EP/S019367/1 and No. EP/P025021/1.

T.T. and I.V.M. proposed and supervised the project. H.W. carried out sample fabrication along with structural and magnetic characterization and data analysis. N.A.B. designed and constructed the ferromagnetic resonance spectrometer. H.W., I.V.M., and T.T. discussed the results and cowrote the manuscript.

## APPENDIX A: FABRICATION METHODS

### 1. Thin-film sample preparation

Fabrication of the samples is accomplished using an AJA ATC 2200-V magnetron sputtering system. The substrates employed are Si/SiO<sub>2</sub> where the oxide layer is 290 nm. No deliberate substrate heating is used. The overall structure of the metal layers is Ta/Co<sub>0.2</sub>Fe<sub>0.6</sub>B<sub>0.2</sub>/Ru/Co<sub>0.2</sub>Fe<sub>0.6</sub>B<sub>0.2</sub> with a Pt or Pd cap employed. The deposition of the Ta, Co<sub>0.2</sub>Fe<sub>0.6</sub>B<sub>0.2</sub>, and Pt layers is done using dc magnetron sputtering from either elemental or, in the case of Co<sub>0.2</sub>Fe<sub>0.6</sub>B<sub>0.2</sub>, alloy targets. The purpose of the Ta is to act as an adhesion layer and to provide a smooth platform off which to grow the film stack. The Ta and Co<sub>0.2</sub>Fe<sub>0.6</sub>B<sub>0.2</sub> are deposited at a power of 20 W, with the cap layer deposited at 100 W. The Ru layer sandwiched in the middle of the Co<sub>0.2</sub>Fe<sub>0.6</sub>B<sub>0.2</sub> layers is deposited through rf sputtering at a power of 75 W. The base pressure prior to deposition is 10<sup>-8</sup> Torr, with no *in situ* magnetic fields applied. The working pressure of the Ar<sup>+</sup> gas is between 3 and 4 mTorr.

## APPENDIX B: CHARACTERIZATION METHODS

### 1. Structure characterization

The structural properties of the layers are determined using X-ray reflectivity. The measurements are carried out using a Rigaku Smart Lab system using a 3 kW Cu K $\alpha$  source. All measurements are performed over a 2 $\theta$  range of 0.1–8.0° with a step size of 0.01°. The data are fitted to a Fresnel model by means of the Parratt recursive algorithm [57] using the GENX simulation package [58]. The fitting is performed until the reduced  $\chi^2$  figure of merit is optimized. This provided information on the thickness, roughness, and density of the constituent layers.

### 2. Magnetic measurements

Magnetization versus applied magnetic field ( $M$ - $H$ ) loops are measured through VSM using a Microsense Model 10 vector VSM. The samples are prepared using a Southbay disk cutter to provide an 8-mm disk for the VSM measurement. These measurements were performed using an in-plane applied magnetic field up to 20 kOe to guarantee saturation of the magnetic domain structure. Background correction is applied by obtaining the linear fit to the saturated region of the hysteresis loop, with its gradient determining the diamagnetic response present.

### 3. Ferromagnetic resonance measurements

The high-frequency properties of the films are determined using a VNA FMR setup. This setup employed a picoprobe waveguide and a Keysight VNA N5224A, which is capable of frequency measurements in the range

10 MHz–43.5 GHz. The probes are contacted to a ground-signal-ground waveguide placed within a magnetic field of up to 1.4 T provided by a GMW electromagnet. As a flip-chip experiment, the sample is placed face down upon the waveguide for characterization, with a natural air barrier sufficient to prevent the shorting of the waveguide. The operating principle of this method is that the magnetic configuration of a film under test will be perturbed by a rf magnetic field due to the electric pulses traversing the waveguide. When the frequency of the perturbation by this small magnetic field is equal to the resonant frequency of the system, a large absorption of this rf energy takes place that causes the transmission of energy through the waveguide (measured through the  $S_{12}$  parameter) to significantly decrease [15,59]. This method is carried out by performing frequency sweeps for a range of applied external fields as opposed to the conventional field sweeps for set frequencies.

- [1] T. Jungwirth, X. Marti, P. Wadley, and J. Wunderlich, Antiferromagnetic spintronics, *Nat. Nanotechnol.* **11**, 231 (2016).
- [2] H. V. Gomonay and V. M. Loktev, Spintronics of antiferromagnetic systems, *Fiz. Nizk. Temp.* **40**, 22 (2014).
- [3] L. Néel, Magnetism and local molecular field, *Science* **174**, 4013 (1971).
- [4] B. N. Engel, J. Akerman, B. Butcher, R. W. Dave, M. DeHerrera, M. Durlam, G. Grynkewich, J. Janesky, S. V. Pietambaran, N. D. Rizzo, and J. M. Slaughter, A 4-Mb toggle MRAM based on a novel bit and switching method, *IEEE Trans. Magn.* **41**, 132 (2005).
- [5] R. Hao, L. Wang, and T. Min, A novel STT-MRAM design with electric-field-assisted synthetic anti-ferromagnetic free layer, *IEEE Trans. Magn.* **55**, 1 (2019).
- [6] P. A. Grünberg, Exchange anisotropy, interlayer exchange coupling and GMR in research and application, sensors actuators, *A Phys.* **91**, 153 (2001).
- [7] J. Walowski and M. Münzenberg, Perspective: Ultrafast magnetism and THz spintronics, *J. Appl. Phys.* **120**, 140901 (2016).
- [8] T. Kampfrath, A. Sell, G. Klatt, A. Pashkin, S. Mährlein, T. Dekorsy, M. Wolf, M. Fiebig, A. Leitenstorfer, and R. Huber, Coherent terahertz control of antiferromagnetic spin waves, *Nat. Photonics* **5**, 31 (2011).
- [9] A. Stupakiewicz, K. Szerenos, D. Afanasiev, A. Kirilyuk, and A. V. Kimel, Ultrafast nonthermal photo-magnetic recording in a transparent medium, *Nature* **542**, 71 (2017).
- [10] D. Bossini and T. Rasing, Femtosecond optomagnetism in dielectric antiferromagnets, *Phys. Scr.* **92**, 024002 (2017).
- [11] A. V. Chumak, V. I. Vasyuchka, A. A. Serga, and B. Hillebrands, Magnon spintronics, *Nat. Phys.* **11**, 453 (2015).
- [12] M. Farle, Ferromagnetic resonance of ultrathin metallic layers, *Reports Prog. Phys.* **61**, 755 (1998).
- [13] V. G. Harris, Modern microwave ferrites, *IEEE Trans. Magn.* **48**, 1075 (2012).

- [14] A. El-Ghazaly, R. M. White, and S. X. Wang, Increasing ferromagnetic resonance frequency using lamination and shape, *J. Appl. Phys.* **117**, 17E502 (2015).
- [15] C. Kittel, On the theory of ferromagnetic resonance absorption, *Phys. Rev.* **73**, 155 (1948).
- [16] C. J. Oates, F. Y. Ogrin, S. L. Lee, P. C. Riedi, G. M. Smith, and T. Thomson, High field ferromagnetic resonance measurements of the anisotropy field of longitudinal recording thin-film media, *J. Appl. Phys.* **91**, 1417 (2002).
- [17] C. Li, G. Chai, C. Yang, W. Wang, and D. Xue, Tunable zero-field ferromagnetic resonance frequency from S to X band in oblique deposited CoFeB thin films, *Sci. Rep.* **5**, 1 (2015).
- [18] T. J. Klemmer, K. A. Ellis, L. H. Chen, B. Van Dover, and S. Jin, Ultrahigh frequency permeability of sputtered Fe-Co-B thin films, *J. Appl. Phys.* **87**, 830 (2000).
- [19] T. Burkert, L. Nordström, O. Eriksson, and O. Heinonen, Giant Magnetic Anisotropy in Tetragonal FeCo Alloys, *Phys. Rev. Lett.* **93**, 027203 (2004).
- [20] E. Van De Riet, W. Klaassens, and F. Roozeboom, On the origin of the uniaxial anisotropy in nanocrystalline soft-magnetic materials, *J. Appl. Phys.* **81**, 806 (1997).
- [21] S. Li, Q. Li, J. Xu, S. Yan, G. X. Miao, S. Kang, Y. Dai, J. Jiao, and Y. Lü, Tunable optical mode ferromagnetic resonance in FeCoB/Ru/FeCoB synthetic antiferromagnetic trilayers under uniaxial magnetic anisotropy, *Adv. Funct. Mater.* **26**, 3738 (2016).
- [22] Y. Fu, Z. Yang, T. Miyao, M. Matsumoto, X. X. Liu, and A. Morisako, Induced anisotropy in soft magnetic Fe<sub>65</sub>Co<sub>35</sub>/Co thin films, *Mater. Sci. Eng. B Solid-State Mater. Adv. Technol.* **133**, 61 (2006).
- [23] N. N. Phuoc, L. T. Hung, and C. K. Ong, Ultra-high ferromagnetic resonance frequency in exchange-biased system, *J. Alloys Compd.* **506**, 504 (2010).
- [24] M. B. Jungfleisch, W. Zhang, and A. Hoffmann, Perspectives of antiferromagnetic spintronics, *Phys. Lett. Sect. A Gen. At. Solid State Phys.* **382**, 865 (2018).
- [25] N. Bhattacharjee, A. A. Sapozhnik, S. Yu. Bodnar, V.Yu. Grigorev, S. Y. Agustsson, J. Cao, D. Dominko, M. Oberfell, O. Gomonay, J. Sinova, M. Kläui, H.-J. Elmers, M. Jourdan, and J. Demsar, Néel Spin-Orbit Torque Driven Antiferromagnetic Resonance in Mn<sub>2</sub>Au Probed by Time-Domain THz Spectroscopy, *Phys. Rev. Lett.* **120**, 237201 (2018).
- [26] S. Baierl, J. H. Mentink, M. Hohenleutner, L. Braun, T.-M. Do, C. Lange, A. Sell, M. Fiebig, G. Woltersdorf, T. Kampfrath, and R. Huber, Terahertz-Driven Nonlinear Spin Response of Antiferromagnetic Nickel Oxide, *Phys. Rev. Lett.* **117**, 197201 (2016).
- [27] D. Bossini, S. Dal Conte, G. Cerullo, O. Gomonay, R. V. Pisarev, M. Borovsak, D. Mihailovic, J. Sinova, J. H. Mentink, Th. Rasing, and A. V. Kimel, Laser-driven quantum magnonics and terahertz dynamics of the order parameter in antiferromagnets, *Phys. Rev. B* **100**, 1 (2019).
- [28] D. Bossini, S. Dal Conte, Y. Hashimoto, A. Secchi, R. V. Pisarev, T. Rasing, G. Cerullo, and A. V. Kimel, Macrospin dynamics in antiferromagnets triggered by sub-20 femtosecond injection of nanomagnons, *Nat. Commun.* **7**, 1 (2016).
- [29] S. Wienholdt, D. Hinzke, and U. Nowak, THz Switching of Antiferromagnets and Ferrimagnets, *Phys. Rev. Lett.* **108**, 247207 (2012).
- [30] David MacNeill, Justin T. Hou, Dahlia R. Klein, Pengxiang Zhang, Pablo Jarillo-Herrero, and Luqiao Liu, Gigahertz Frequency Antiferromagnetic Resonance and Strong Magnon-Magnon Coupling in the Layered Crystal CrCl<sub>3</sub>, *Phys. Rev. Lett.* **123**, 047204 (2019).
- [31] T. Chiba, G. E. W. Bauer, and S. Takahashi, Magnetization damping in noncollinear spin valves with antiferromagnetic interlayer couplings, *Phys. Rev. B* **92**, 054407 (2015).
- [32] R. A. Duine, K. J. Lee, S. S. P. Parkin, and M. D. Stiles, Synthetic antiferromagnetic spintronics, *Nat. Phys.* **14**, 217 (2018).
- [33] P. Bruno and C. Chappert, Oscillatory Coupling Between Ferromagnetic Layers Separated by a Nonmagnetic Metal Spacer, *Phys. Rev. Lett.* **67**, 1602 (1991).
- [34] S. S. P. Parkin and D. Mauri, Spin engineering: Direct determination of the Ruderman-Kittel-Kasuya-Yosida far-field range function in ruthenium, *Phys. Rev. B* **44**, 7131 (1991).
- [35] R. Coehoorn, Period of oscillatory exchange interactions in Co/Cu and Fe/Cu multilayer systems, *Phys. Rev. B* **44**, 9331 (1991).
- [36] S. Li, G. X. Miao, D. Cao, Q. Li, J. Xu, Z. Wen, Y. Dai, S. Yan, and Y. Lü, Stress-Enhanced interlayer exchange coupling and optical-mode FMR frequency in self-bias FeCoB/Ru/FeCoB trilayers, *ACS Appl. Mater. Interfaces* **10**, 8853 (2018).
- [37] S. Li, C. Wang, X. M. Chu, G. X. Miao, Q. Xue, and W. Zou, Engineering optical mode ferromagnetic resonance in FeCoB films with ultrathin Ru insertion, *Sci. Rep.* **6**, 33349 (2016).
- [38] S. V. Pietambaram, J. Janesky, R. W. Dave, J. J. Sun, G. Steiner, and J. M. Slaughter, Exchange coupling control and thermal endurance of synthetic antiferromagnet structures for MRAM, *IEEE Trans. Magn.* **40**, 2619 (2004).
- [39] H. A. M. van den Berg, W. Clemens, G. Gieres, G. Rupp, M. Vieth, J. Wecker, and S. Zoll, GMR angle detector with an artificial antiferromagnetic subsystem (AAF), *J. Magn. Magn. Mater.* **165**, 524 (1997).
- [40] K. O. Z. Zhang and P. E. Wigan, FMR in strongly coupled Co/Ru/Co structures, *IEEE Trans. Magn.* **29**, 2717 (1993).
- [41] L. Zhang, W. Zhang, X. Liu, Y. Wang, J. Bai, D. Wei, and F. Wei, High frequency characteristics of synthetic antiferromagnetic coupling FeCoN sandwich films, *IEEE Trans. Magn.* **47**, 3932 (2011).
- [42] X. G. Xu, D. L. Zhang, X. Q. Li, J. Bao, Y. Jiang, and M. B. A. Jalil, Synthetic antiferromagnet with heusler alloy Co<sub>2</sub>FeAl ferromagnetic layers, *J. Appl. Phys.* **106**, 123902 (2009).
- [43] I. Kim, J. Kim, K. H. Kim, and M. Yamaguchi, Effects of boron contents on magnetic properties of Fe-Co-B thin films, *IEEE Trans. Magn.* **40**, 2706 (2004).
- [44] A. Yang, H. Imrane, J. Lou, J. Kirkland, C. Vittoria, N. Sun, and V. G. Harris, Effects of boron addition to the atomic structure and soft magnetic properties of FeCoB films, *J. Appl. Phys.* **103**, 07E736 (2008).
- [45] M. Namikawa, M. Munakata, S.-I. Aoqui, and M. Yagi, B content dependence on anisotropy field of CoFeB thin

- film for GHz frequency use, *IEEE Trans. Magn.* **41**, 37 (2005).
- [46] P. Bruno, Theory of interlayer exchange interactions in magnetic multilayers, *J. Phys. Condens. Matter* **11**, 9403 (1999).
- [47] J. Wecker, G. Reiss, T. Dimopoulos, H. Brückl, N. Wiese, and M. Rührig, Antiferromagnetically coupled CoFeB/Ru/CoFeB trilayers, *Appl. Phys. Lett.* **85**, 2020 (2004).
- [48] B. Heinrich, J. F. Cochran, M. Kowalewski, J. Kirschner, Z. Celinski, A. S. Arrott, and K. Myrtle, Magnetic anisotropies and exchange coupling in ultrathin fcc Co(001) structures, *Phys. Rev. B* **44**, 9348 (1991).
- [49] C. Wang, S. Zhang, S. Qiao, H. Du, X. Liu, R. Sun, X. M. Chu, G. X. Miao, Y. Dai, S. Kang, S. Yan, and S. Li, Dual-mode ferromagnetic resonance in an FeCoB/Ru/FeCoB synthetic antiferromagnet with uniaxial anisotropy, *Appl. Phys. Lett.* **112**, 192401 (2018).
- [50] S. M. Rezende, C. Chesman, M. A. Lucena, A. Azevedo, F. M. De Aguiar, and S. S. P. Parkin, Studies of coupled metallic magnetic thin-film trilayers, *J. Appl. Phys.* **84**, 958 (1998).
- [51] P. E. Wigen, Z. Zhang, L. Zhou, M. Ye, and J. A. Cowen, The dispersion relation in antiparallel coupled ferromagnetic films, *J. Appl. Phys.* **73**, 6338 (1993).
- [52] K. J. Lee, M. D. Stiles, H. W. Lee, J. H. Moon, K. W. Kim, and S. W. Lee, Self-consistent calculation of spin transport and magnetization dynamics, *Phys. Rep.* **531**, 89 (2013).
- [53] H. Yang, Y. Li, and W. E. Bailey, Large spin pumping effect in antisymmetric precession of Ni<sub>79</sub>Fe<sub>21</sub>/Ru/Ni<sub>79</sub>Fe<sub>21</sub>, *Appl. Phys. Lett.* **108**, 242404 (2016).
- [54] See Supplemental Material at <http://link.aps.org/supplemental/10.1103/PhysRevApplied.13.034035> for evidence of a small in-plane uniaxial anisotropy in Co<sub>0.2</sub>Fe<sub>0.6</sub>B<sub>0.2</sub> thin films.
- [55] A. T. Hindmarch, A. W. Rushforth, R. P. Campion, C. H. Marrows, and B. L. Gallagher, Origin of in-plane uniaxial magnetic anisotropy in CoFeB amorphous ferromagnetic thin films, *Phys. Rev. B - Condens. Matter Mater. Phys.* **83**, 212404 (2011).
- [56] J. P. Nibarger, R. Lopusnik, Z. Celinski, and T. J. Silva, Variation of magnetization and the landé g factor with thickness in Ni-Fe films, *Appl. Phys. Lett.* **83**, 93 (2003).
- [57] L. G. Parratt, Surface studies of solids, *Phys. Rev.* **95**, 359 (1954).
- [58] M. Björck and G. Andersson, Genx: An extensible X-ray reflectivity refinement program utilizing differential evolution, *J. Appl. Crystallogr.* **40**, 1174 (2007).
- [59] I. S. Maksymov and M. Kostylev, Broadband stripline ferromagnetic resonance spectroscopy of ferromagnetic films, multilayers and nanostructures, *Phys. E Low-Dimensional Syst. Nanostructures* **69**, 253 (2015).